PAPER

# Electronic structure of the substitutional vacancy in graphene: density-functional and Green's function studies

New Journal of Physics
The open access journal for physics

# Corrigendum: Electronic structure of the substitutional vacancy in graphene: density-functional and Green's function studies

2012 *New J. Phys.* **14** 083004

**B R K Nanda**[1], **M Sherafati**[2], **Z S Popović**[3] **and S Satpathy**[2,4]

[1] Department of Physics, Indian Institute of Technology Madras, Chennai 600036, India

[2] Department of Physics & Astronomy, University of Missouri, Columbia, MO 65211, USA

[3] Institute of Nuclear Sciences, Vinča, University of Belgrade, P. O. Box 522, 11001 Belgrade, Serbia

E-mail: satpathys@missouri.edu

*New Journal of Physics* **15** (2013) 039501 (2pp)
Received 20 February 2013
Published 13 March 2013
Online at http://www.njp.org/
doi:10.1088/1367-2630/15/3/039501

In the original paper, figure 12(b) was incorrect and the caption of figure 12 was also erroneous. The correct figure and caption are shown below.

[4] Author to whom any correspondence should be addressed.

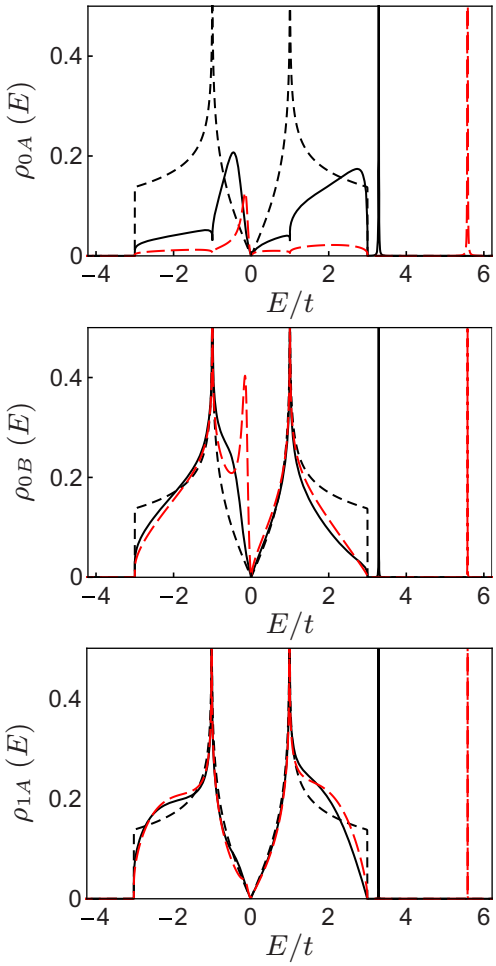


**Figure 12.** LDOS at the impurity site $\rho_{0A}$ (top), the NN site $\rho_{0B}$ (middle) and the next-NN site $\rho_{1A}$ (bottom) obtained from equations (13) and (14) for different strengths of the impurity potential $U_0/t = 0$, 2 and 5, denoted by black dashed, black solid and red dashed lines, respectively. As $U_0 \to \infty$, the top LDOS goes to zero (except for the bound state beyond the top of the band whose energy goes to $\infty$), and the zero-mode state lives only on the $B$ sublattice, as indicated from the middle and the bottom panels. The prominent zero-mode peak in the middle panel for $U_0/t = 5$ will develop into a $\delta$-function peak at $E = 0$ as the impurity potential $U_0 \to \infty$.

New Journal of Physics
The open-access journal for physics

# Electronic structure of the substitutional vacancy in graphene: density-functional and Green's function studies

**B R K Nanda[1], M Sherafati, Z S Popović[2] and S Satpathy[3]**
Department of Physics and Astronomy, University of Missouri, Columbia, MO 65211, USA
E-mail: satpathys@missouri.edu

*New Journal of Physics* **14** (2012) 083004 (25pp)
Received 18 March 2012
Published 3 August 2012
Online at http://www.njp.org/
doi:10.1088/1367-2630/14/8/083004

**Abstract.** We study the electronic structure of graphene with a single substitutional vacancy using a combination of the density-functional, tight-binding and impurity Green's function approaches. Density-functional studies are performed with the all-electron spin-polarized linear augmented plane wave (LAPW) method. The three $sp^2\sigma$ dangling bonds adjacent to the vacancy introduce localized states ($V\sigma$) in the mid-gap region, which split due to the crystal field and a Jahn–Teller distortion, while the $p_z\pi$ states introduce a sharp resonance state ($V\pi$) in the band structure. For a planar structure, symmetry strictly forbids hybridization between the $\sigma$ and the $\pi$ states, so that these bands are clearly identifiable in the calculated band structure. As to the magnetic moment of the vacancy, the Hund's rule coupling aligns the spins of the four localized $V\sigma_1 \uparrow\downarrow$, $V\sigma_2 \uparrow$ and $V\pi \uparrow$ electrons, resulting in an $S = 1$ state, with a magnetic moment of $2\mu_B$, which is reduced by about $0.3\mu_B$ due to the anti-ferromagnetic spin polarization of the $\pi$ band itinerant states in the vicinity of the vacancy. This results in the net magnetic moment of $1.7\mu_B$. Using the Lippmann–Schwinger equation, we reproduce the well-known $\sim 1/r$ decay of the localized $V\pi$ wave function with distance, and in addition, find an

[1] Permanent address: Department of Physics, Indian Institute of Technology Madras, Chennai 600036, India.
[2] Permanent address: Institute of Nuclear Sciences, Vinča, University of Belgrade, PO Box 522, 11001 Belgrade, Serbia.
[3] Author to whom any correspondence should be addressed.

interference term coming from the two Dirac points, previously unnoticed in the literature. The long-range nature of the $V\pi$ wave function is a unique feature of the graphene vacancy and we suggest that this may be one of the reasons for the widely varying relaxed structures and magnetic moments reported from the supercell band calculations in the literature.

**Contents**



## 1. Introduction

Graphene is a material of considerable interest on account of its unusual linearly dispersive Dirac band structure and particle–hole symmetry [1, 2]. The vacancy constitutes an important defect center, the electronic structure of which forms the basic foundation for understanding the behavior of more complex defects including impurities. Recently, it was suggested that transition-metal-doped graphene with vacancies may have potential application in hydrogen storage [3]. Experimentally, vacancies in graphene have been created intentionally by irradiating materials with electrons and ions [4–7], and may also occur at small concentration during the growth process [8]. Although an ideal graphene sheet is non-magnetic, experimental observation of magnetism in carbon systems has been long explained in terms of a variety of defects including isolated vacancies, vacancy clusters or the presence of internal or external boundaries as in nanoribbons [7, 9–11].

There have been several theoretical studies of the isolated vacancy in graphene from first-principles density-functional theory (DFT) [12–22] or Hartree–Fock calculations [23] as well as from tight-binding models [25–27]. There is also a large amount of related work on chemisorbed defects such as hydrogen defects and chemisorbed magnetic atoms (see, e.g., [13] and [28]). Most of the tight-binding models have focused on the $\pi$ bands alone, which is clearly inadequate due to the formation of $sp^2\sigma$ dangling bonds in the mid-gap region. The

first-principles calculations include all relevant states in the band structure including the $sp^2\sigma$ states; however, in spite of all these works, a clear picture of the vacancy states has not emerged.

In this paper, we study the electronic structure of the vacancy in graphene using the all-electron density-functional linear augmented plane waves (LAPW) method along with tight-binding studies as well as the impurity Green's function (GF) approach to interpret the band structure. To our knowledge, this is the first all-electron density-functional calculation for the vacancy in graphene reported in the literature. We have already reported the electronic structure for mono- and bilayer graphene using the same method [29]. In addition to the DFT calculations, the nature of the vacancy-induced states is modeled from the tight-binding and GF studies, which help interpret the DFT results.

The basic overall picture of the electronic structure that emerges from our present work is summarized in figure 1. It shows the standard $\sigma$ and $\pi$ bands of graphene plus the vacancy-induced states, denoted by $V\pi$ and $V\sigma$, which are split due to the crystal field, Jahn–Teller and the Hund's rule interactions. The $V\sigma$ states are made of three $sp^2\sigma$ dangling bond states, which are located on the three carbon atoms adjacent to the vacancy with their lobes directed toward the vacancy site. With their bonding partners missing, they occur in the mid-gap region. At the same time, a localized state $V\pi$ gets introduced in the $\pi$ bands in the mid-gap region as well, the so-called 'zero-mode' state, whose energy is exactly zero in the nearest-neighbor (NN) tight-binding approximation. These four states, localized around the vacancy center, can hold eight electrons in total taking into account the spin degeneracy. The level structure of the vacancy-induced states is shown in figure 2.

At the same time, electron counting arguments show that the vacancy releases four electrons to be occupied among the above localized states. These electrons include the three orphan $sp^2\sigma$ electrons, one from each of the three carbon atoms adjacent to the vacancy, plus one orphan $\pi$ electron, whose origin may be understood in the following way. Focusing on the $\pi$ states now and considering a vacancy on the $A$ sublattice, the majority sublattice $B$ has one extra atom, $N_B - N_A = 1$, so that the total number of $\pi$ orbitals is $N_A + N_B$, which is the same as $2N_A + 1$. Out of these, there is one zero-mode state and the electron–hole symmetry of the graphene lattice results in $N_A$ band states below $E = 0$ and the same number above it. (See figure 7 for the $\pi$ band structure.) So, of the $2N_A + 1$ $\pi$ electrons (one per atom), $2N_A$ fill up the lower bands, leaving a lone orphan $\pi$ electron. These four orphan electrons (three $\sigma$ and one $\pi$) occupy the vacancy-induced states as indicated in figure 1.

The remaining sections are organized as follows. In section 2, we discuss the results of our DFT calculations. Section 3 discusses the crystal-field and Jahn–Teller splitting of the vacancy-induced localized $\sigma$ states and section 4 is devoted to the vacancy-induced $\pi$ states. In section 4.1, we revisit the zero-mode theorem, and in section 4.2, we present numerical results for the $\pi$ states from a numerical diagonalization of the tight-binding Hamiltonian before discussing the vacancy-induced $\pi$ states using the GF approach in sections 4.3 and 4.4. Finally, the results are summarized in section 5.

## 2. Density-functional calculations

For the density-functional calculations, we used the all-electron spin-polarized LAPW method [30] with the general gradient approximation (GGA) [31] for the exchange-correlation functional. A 72-atom $6 \times 6$ supercell was used, which included one vacancy site. The LAPW-basis functions included the carbon 2s and 2p valence orbitals and a momentum cutoff of

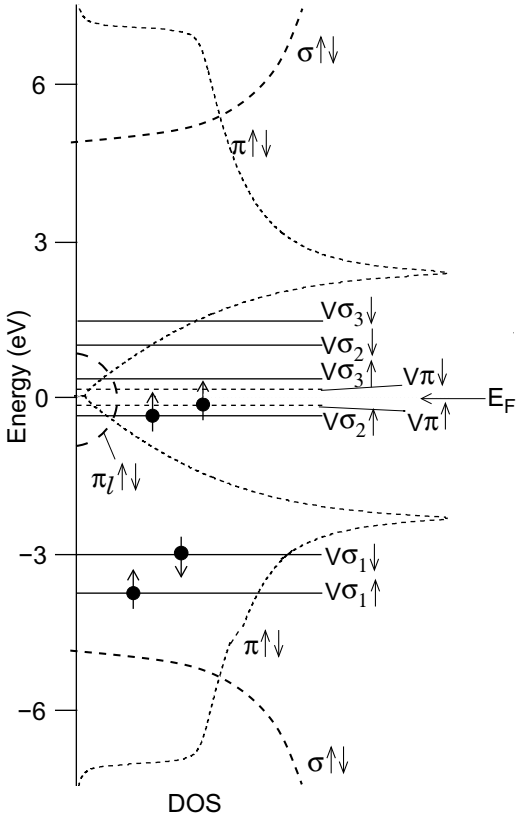


**Figure 1.** Sketch of the electronic structure of an isolated substitutional vacancy in graphene. The continuum $\pi$ and $\sigma$ bands are shown as dashed curves, while the vacancy-induced localized states, $V\sigma$ and $V\pi$, are indicated by straight lines. $E_F$ is the Fermi energy. The occupied vacancy states are indicated by solid circles with a corresponding net magnetic moment of $2\mu_B$. The circular density of states (DOS) in the mid-gap region, labeled $\pi_l \uparrow\downarrow$, indicates schematically the antiferromagnetic spin polarization of the $\pi$ electron states in the *local* neighborhood of the vacancy. This spin polarization is responsible for the reduction of the localized magnetic moment from $2\mu_B$ ($S = 1$) to about $1.7\mu_B$ in our density-functional calculation.

$RK_{max} = 5.2$ was used, with approximately 3500 basis functions and about 50 000 plane waves at each $k$ point. All atomic sphere radii were taken as 0.66 Å. The maximum angular momentum for the wave function expansion inside the atomic sphere was kept at $l_{max} = 6$. Thirty $k$ points in the irreducible Brillouin zone were found to be sufficient for converged results in the self-consistent calculations.

### *2.1. Relaxed structure*

First we performed a structural optimization of the lattice constant for pure graphene, which yielded about the same lattice constant as the experimental value. For the vacancy calculation, the lattice constant was kept fixed at the experimental value and a structural relaxation was performed for the entire structure. The optimization yielded a planar Jahn–Teller distorted

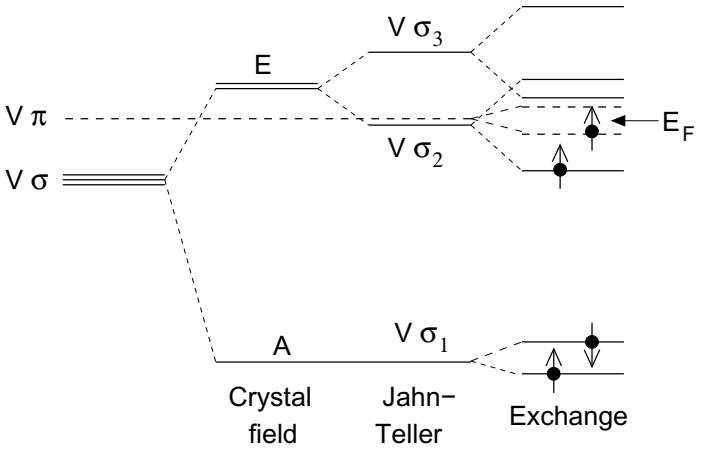


**Figure 2.** Splitting of the three dangling bond $sp^2\sigma$ states of the carbon triangle, denoted by $V\sigma$, and the vacancy-induced zero-mode $V\pi$ state originating from the $\pi$ band. The splitting of the $V\sigma$ states is discussed in detail in section 3.

carbon triangle around the vacancy with the carbon atoms outside the triangle relaxed by a much smaller amount. For the carbon triangle, we found two long bonds of length 2.66 Å each and a short bond of length 2.40 Å (figure 3), as compared with the 2.48 Å for the undistorted structure. In terms of the standard Jahn–Teller modes of the equilateral triangle, the magnitudes of the distortion are: $Q_0 = 0.08$ Å (breathing mode), $Q_1 = 0.166$ Å (symmetric bond-bending mode) and $Q_2 = 0$ (asymmetric mode) [32].

The relaxed structure for the vacancy reported in the literature varies widely. While some have reported planar structures [13–17, 23], others have found non-planar structures with out-of-plane displacements varying from $\delta z \approx 0.12$ to 0.47 Å [12, 19–22]. We find that a paramagnetic relaxation (less accurate for the present problem) yields a non-planar structure $\delta z \approx 0.27$ Å, whereas a spin-polarized calculation yields a planar structure, an observation made by Faccio *et al* [17] from their calculations as well using the SIESTA code. We attribute this wide variation in the calculated relaxed structure in the literature partly to the unusual nature of the $V\pi$ bound state, which falls off only as $1/r$, leading to a larger width of the $V\pi$ band in the supercell calculations than is expected from resonance broadening due to the $\pi$ band continuum.

The calculated vacancy formation energies agree much better between different calculations. Our result for $E_V = E(\text{graphene} + \text{vacancy}) - N^{-1}(N-1)E(\text{graphene})$, $N$ being the number of atoms in the graphene supercell, is 7.87 eV, which compares well with the previous calculations [12, 15, 20] of 7.4–7.8 eV as well as with the experimental value of $7.0 \pm 0.5$ eV [33].

### 2.2. *Electronic structure*

Figure 4 shows the band structure, where the vacancy-induced $V\sigma$ and $V\pi$ states are clearly seen. The momentum points in the Brillouin zone for the band structure plot are defined as: $K = \hat{x}/\sqrt{3} + \hat{y}$ and $M = \hat{y}$ in units of $2\pi 3^{-1}a^{-1}/n$ with $n = 6$ for the $6 \times 6$ supercell used in the calculation. For this supercell, it can be easily seen by drawing both the Brillouin zones that the Dirac points $K$ and $K'$ of graphene get folded into the $\Gamma$ point of the supercell Brillouin

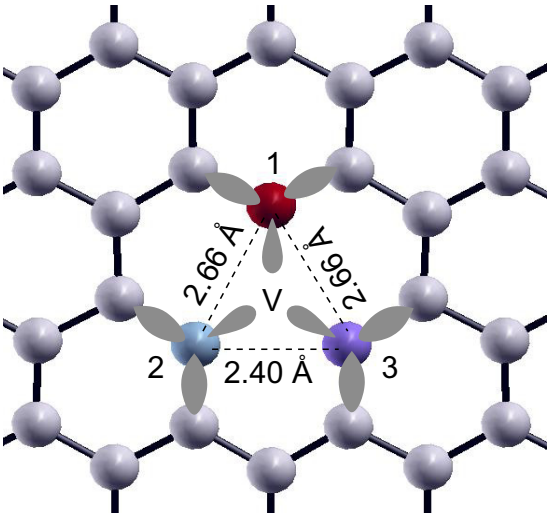


**Figure 3.** The Jahn–Teller distorted planar carbon triangle obtained from structural relaxation using the all-electron spin-polarized LAPW–GGA method.

zone, so that remnants of the Dirac bands are seen at the Γ point in figure 4 just above $E_F$ (see also figure 7 for the folded graphene tight-binding $\pi$ bands for the same supercell and note the similarity between the tight-binding $\pi$ bands and the DFT bands, figure 4). Due to symmetry, the $\sigma$ and $\pi$ bands do not mix (strictly forbidden for the planar geometry, but also weakened significantly if the relaxed geometry is non-planar), which leads to clearly identifiable vacancy-induced $V\sigma$ bands. The $V\sigma$ states originating from the dangling bonds are split due to the crystal field, Jahn–Teller and exchange coupling as indicated in figure 2 and discussed in more detail in section 3. The dispersion of the $V\sigma$ bands in the band structure comes from the vacancy–vacancy interactions in different supercells or from the $k$-dependent interaction with the bonding and the anti-bonding $\sigma$ bands, both effects being small. For non-planar relaxed structure, they should have a small resonance broadening due to the interaction with the $\pi$ band continuum. Three electrons occupy these states, leading to the occupation $V\sigma_1 \uparrow\downarrow$, $V\sigma_2 \uparrow$, with the remaining fourth electron occupying the $V\pi \uparrow$ state.

We now turn to a description of the effect of the vacancy on the $\pi$ states. Basically, the vacancy introduces a sharp, resonance state $V\pi$ in the mid-gap region. The following summarizes the discussions of section 4, which are important to keep in mind: (i) if only NN tight-binding hoppings are kept, then the vacancy introduces a single localized state $V\pi$ at $E = 0$ and of zero width called the zero-mode state, and its wave function decays as $\sim 1/r$ with distance in the linear-band approximation. (ii) The presence of the vacancy in each supercell does not affect the energy or the width of this state because of the result that the zero-mode wave function lives on the majority sublattice entirely and any changes in the minority sublattice do not affect it (in the supercell, all vacancies are located on the same minority sublattice). (iii) However, due to the second-neighbor (2NN) hopping as well as the exchange splitting, the energy of $V\pi$ is different from zero, so that it now has a small but finite width due to resonance broadening with the linear $\pi$ band continuum consistent with the scanning tunneling microscopy experiments [10]. (iv) In the supercell calculations, the $V\pi$ state acquires an extra broadening due to the slow $1/r$ decay of the $V\pi$ wave function, because of the interaction between the supercells.

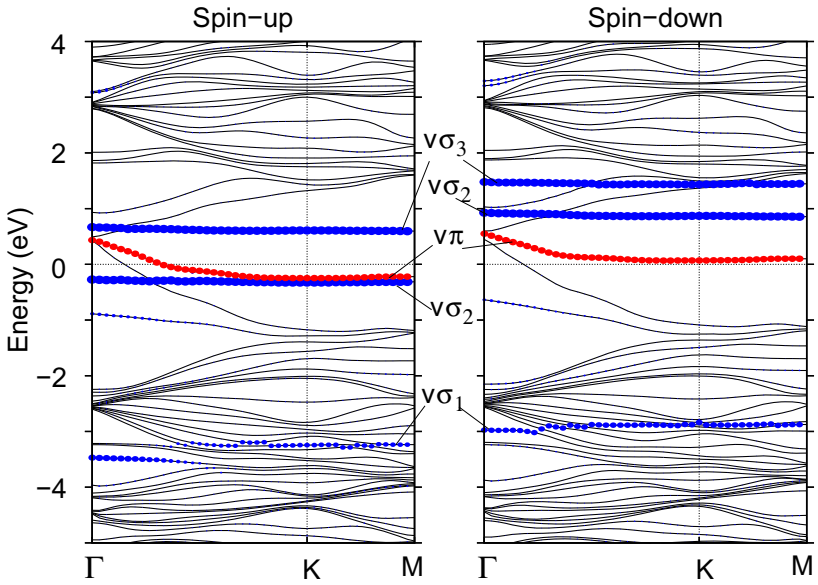


**Figure 4.** Spin-polarized band structure of graphene with a single vacancy in a 72-atom $6 \times 6$ supercell obtained from the density-functional LAPW method. The vacancy-induced $V\sigma$ and $V\pi$ bands are indicated in blue and red, respectively. Symmetry strictly forbids the admixture between $\sigma$ and $\pi$ states for a planar relaxation around the vacancy, leading to flat $V\sigma$ bands (blue lines). The $V\pi$ bands are not flat owing to hybridization with the continuum $\pi$ states. The Dirac points $K$ and $K'$ of the original graphene Brillouin zone get folded into the $\Gamma$ point of the supercell Brillouin zone. The zero of energy is taken to be the Fermi energy $E_F$.

### *2.3. Dirac point*

In figure 4, the Dirac point occurs above the $E_F$ (see the bands just above $E_F$ at the $\Gamma$ point, to which the standard Dirac points $K$ and $K'$ have become folded). For the truly isolated vacancy, the location of the Dirac point above $E_F$ would mean that an infinite number of electrons are transferred from the unfilled part of the Dirac cones to the lone vacancy site, which is impossible. Another way of seeing this is to consider first an infinite lattice without the vacancy. Obviously, the $E_F$ occurs at the Dirac point with zero DOS as usual. Now, if we introduce a single vacancy into the structure it can only affect the position of $E_F$ by $\sim 1/N$, where $N$ is the total number of atoms in the lattice, so that $E_F$ remains unchanged for the infinite lattice. Of course, the electron states in the local neighborhood of the vacancy are modified, e.g. due to the resonance interaction with the vacancy states or due to the vacancy potential. The Dirac-like bands seen just above $E_F$ at $\Gamma$ in figure 4 represent the effect of the vacancy on the electronic structure in the local neighborhood of the vacancy in the supercell calculation.

### *2.4. Magnetic moment*

The vacancy magnetic moment consists of two parts as shown schematically in figure 5: (i) the localized moment coming from the vacancy states $V\pi$ and $V\sigma$ and (ii) the induced moment

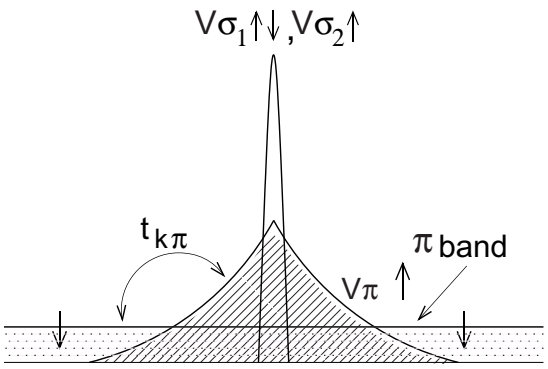


**Figure 5.** Sketch of the magnetic moment for an isolated vacancy, emphasizing the spatial extent of the various electronic states. The $V\sigma$ electrons are highly localized on the carbon triangle surrounding the vacancy, whereas the $V\pi$ electron is only 'quasi-localized' with its wave function decaying only as $1/r$. Hund's-rule exchange aligns the $V\sigma$ and $V\pi$ electrons, producing an $S = 1$ state with the nominal magnetic moment of $2\mu_B$. This moment is, however, reduced by polarization of the $\pi$ band spins in the vicinity of the vacancy, described by an antiferromagnetic Kondo-like coupling $t_{k\pi}$ between the $\pi$ bands and the localized $V\pi$ and $V\sigma$ moments. The $\pi$ band polarization is about $0.3\mu_B$ in our DFT calculations, leading to the net magnetic moment of $1.7\mu_B$.

on the band electrons in the vicinity of the vacancy. One can argue on general grounds that the first contribution should be $2\mu_B$ ($S = 1$), while the second contribution should reduce this value somewhat due to the antiferromagnetic Kondo-like coupling between the localized and the itinerant band spins. Turning to the localized states, the vacancy leaves four electrons to be occupied among the $V\sigma$ dangling bond states and the $V\pi$ zero-mode state. Of these, three electrons will occupy the $V\sigma$ states, so that one electron resides on each of the three dangling bonds of the carbon triangle. The Coulomb interaction $U$ would prevent the occupation of a fourth $V\sigma$ state, so that the remaining electron is energetically favored to occupy the $\pi$ states. Hund's coupling between the $V\sigma$ and $V\pi$ electrons leads then to an $S = 1$ state with a magnetic moment of $2\mu_B$. This basic picture is illustrated in figures 2 and 5 and is fully supported by the DFT bands (figure 4). This localized magnetic moment of $2\mu_B$ is reduced due to the spin polarization of the $\pi$ bands in the vicinity of the vacancy.

The spin polarization of the $\pi$ bands can occur due to two factors: (i) the resonance coupling with the $V\pi\uparrow$ electron with the $\pi$ continuum bands and (ii) the Kondo-like antiferromagnetic interaction between the localized vacancy states and the continuum $\pi$ states. The first is not well described in a supercell calculation due to the long-range nature of the $V\pi$ state and the second effect is intrinsically not well described within the band theory.

Our DFT calculations yield a magnetic moment of about $1.7\mu_B$. This can be seen by estimating the number of holes in the small hole pocket in the two bands just above $E_F$ at the $\Gamma$ point in the spin-up bands of figure 4. The spin-down bands must contain exactly the same number of extra electrons missing from the spin-up bands. Without this pocket of holes, which represents the band polarization in the immediate neighborhood of the vacancy, the magnetic moment would be exactly $2\mu_B$, corresponding to the full occupancy of $V\sigma_1\uparrow\downarrow$, $V\sigma_2\uparrow$ and $V\pi\uparrow$. The existence of the hole pocket reduces this number. We can estimate the number $n$ in the hole

pocket by computing the total area of the two-hole Fermi surfaces and comparing it to the area of the supercell Brillouin zone, which yields the value $n \approx 0.15$. Since the same number of electrons must be accommodated in the spin-down bands, this would cause a net reduction of $N_\uparrow - N_\downarrow$ by 0.30, leading to a net magnetic moment of $1.7\mu_B$.

In the literature, the calculated magnetic moment varies widely, anywhere between 1.04 and $1.84\mu_B$ [12–24]. Typically, the lower values come from calculations, where the $V\pi\uparrow$ and $V\pi\downarrow$ bands overlap significantly. We suggest that the variation of the calculated magnetic moment in the literature is due to the intrinsic deficiency of the supercell method in estimating the $\pi$ magnetic moment due to the slow $1/r$ decay of the $V\pi$ state, which produces an extra broadening of the $V\pi$ state due to the supercell interaction and does not take into account the full anti-ferromagnetic polarization of the itinerant $\pi$ band states.

The exchange splitting $\Delta$ of the $V\pi$ state is due to its overlap with the $V\sigma$ states which are localized on the three carbon atoms adjacent to the vacancy. It may be estimated from the expression

$$\Delta \equiv E(V\pi_\downarrow) - E(V\pi_\uparrow) \approx J_H \times |\Psi_0|^2 \approx 0.35\,\text{eV}, \tag{1}$$

where the Hund's rule energy is typically $J_H \sim 0.9$–$1.0\,\text{eV}$ for the atoms and $|\Psi_0|^2 \sim 0.4$ is the combined total density of the $V\pi$ state on the carbon triangle as obtained from the DFT results. The estimated exchange splitting is in agreement with the splitting seen in the DFT bands (figure 4).

### *2.5. Relation to Lieb's theorem*

Lieb's theorem [34] states that for the repulsive one-band Hubbard model on a bipartite lattice and half-filled band, the ground state has spin $S = (1/2)|N_B - N_A|$, $N_A$ ($N_B$) being the number of sites on the two sublattices. It is important to point out that the theorem holds if we consider only the $\pi$-band system and also neglect the small 2NN interactions that couple the two sublattices. Thus, with a single vacancy present, $|N_B - N_A| = 1$ so that according to Lieb's theorem we should have a net spin of $S = 1/2$. However, in addition to the $\pi$, we also have the $\sigma$ electrons. The Lieb result of $S = 1/2$ for the $\pi$ electrons is now coupled to the spins of the three $\sigma$ electrons localized near the vacancy, leading to the net spin $S = 1$ as indicated in the summary figure (figure 1). We have already argued that the magnetic moment of $2\mu_B$ corresponding to $S = 1$ will be reduced due to the polarization of the band electrons in the local neighborhood of the vacancy.

## 3. Vacancy-induced $V\sigma$ states

The essential features of the density-functional results may be understood by simple tight-binding considerations of the effect of the vacancy on the $\sigma$ and the $\pi$ bands. We study the $\sigma$ states in this section followed by the $\pi$ states in the next section.

The description of the vacancy-induced $V\sigma$ states for graphene is rather simple. In graphene, the $sp^2\sigma$ states are removed away from $E_F$ due to strong interaction with neighboring orbitals along the C–C bonds. However, with a vacancy present, the three $sp^2\sigma$ orbitals of the three NN carbon atoms with their lobes pointed toward the vacancy have their usual bonding partners missing, so that they occur near $E_F$, with their on-site energies $\epsilon_\sigma$ slightly below the $\pi$ orbital energies because of the s orbital component present in the $\sigma$ states.

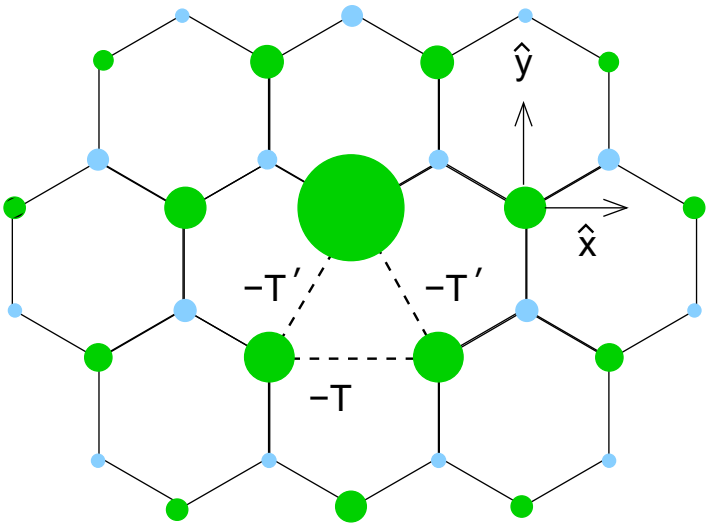


**Figure 6.** Spin density $n_\uparrow - n_\downarrow$ at different sites in graphene with a vacancy as obtained from the density-functional calculations. Green (blue) circles indicate positive (negative) values, with the area of the circle being proportional to the spin density. The spin moments on the carbon atoms other than the vacancy triangle are due to the $\pi$ electrons, which are long-range due to the slow $1/r$ decay of the $V\pi$ state. The hopping integrals $T$ and $T'$ between the $sp^2\sigma$ orbitals on the carbon triangle adjacent to the vacancy have reference to the model discussed in section 3.

The crystal-field splitting, however, will lift the threefold degeneracy. The main feature can be described by taking into account the 2NN hopping $T$ between the three dangling bonds in the undistorted triangle, leading to the $3 \times 3$ Hamiltonian:

$$H_{\mathrm{cf}} = \begin{pmatrix} \epsilon_\sigma & -T & -T \\ -T & \epsilon_\sigma & -T \\ -T & -T & \epsilon_\sigma \end{pmatrix}, \tag{2}$$

diagonalization of which yields a double degenerate state at $E = T$ and a single degenerate state at $E = -2T$ as shown in figure 2, where we call this splitting the crystal-field splitting. The Jahn–Teller distortion of the triangle splits the double degenerate state further, which is described by the unequal hopping $T \neq T'$. Taking the isosceles-triangle relaxation found in our DFT results, two of the three hopping terms are modified into $T'$ as indicated in figure 6. From the DFT band structure, we find that $T \approx 1.6\,\mathrm{eV}$, while $T' \approx 1.2\,\mathrm{eV}$. The new eigenstates are: $E_{\sigma_1,\sigma_2} = 2^{-1}(-T \mp \sqrt{8T'^2 + T^2})$ and $E_{\sigma_3} = T$ with the corresponding (unnormalized) wave functions $\Psi_{1,2} = ((-T \pm \sqrt{8T'^2 + T^2})/T', 1, 1)$ and $\Psi_3 = (0, -1, 1)$. This simple model suggests a Jahn–Teller distortion of the carbon triangle surrounding the vacancy.

The Jahn–Teller interaction is of the type $E \otimes e$ (both electronic and vibrational states are doubly degenerate) in a trigonal ($D_{3h}$) symmetry. With this lattice distortion, the trigonal symmetry is broken. The distortion removes the double degeneracy and the two states (shown in figure 2 as $V\sigma_2$ and $V\sigma_3$) are now split by the amount $2^{-1}(3\,T - \sqrt{8T'^2 + T^2}) \approx 4(T - T')/3 \approx 0.55\,\mathrm{eV}$. Since there are only three electrons available to the $V\sigma$ states, $V\sigma_1$ is occupied by two electrons, while the lone remaining electron occupies the $V\sigma_2$ state. The spin degeneracy

is removed by Hund's coupling with the electron occupying the $V\pi$ state, producing the spin structure indicated in figure 2. The wave function $\Psi_2$ corresponding to the $V\sigma_2$ state shows that the maximum weight ($\sim$66%) comes from the $sp^2\sigma$ dangling orbital of the apical atom of the carbon triangle, which is consistent with the spin density plotted in figure 6. The Jahn–Teller distortion is actually dynamic, with the carbon triangle tunneling between three equivalent minima on the adiabatic potential surface of the $E \otimes e$ Jahn–Teller problem, an issue we discuss elsewhere [35].

## 4. Vacancy-induced $V\pi$ states

In this section, we discuss the origin of the localized state—the so-called 'zero-mode' state—near the band center of the $\pi$ bands. Understanding the origin and 'quasi-localized' nature of the zero-mode state is an essential part of the interpretation of the full band calculation using DFT.

If NN interactions alone are present, the 'zero-mode' state is a localized state with energy exactly at the band center. If, in addition, higher-neighbor interactions are also present but not too large, as is the case for graphene [29], then the localized state turns into a sharply peaked resonance state owing to its overlap with $\pi$ bands and occurs not too far away from the band center.

### *4.1. The existence of the zero-mode state*

According to the zero-mode theorem [25], which is in fact valid for any bipartite lattice with NN interactions, whenever there is an imbalance in the number of atoms in the two sublattices of a bipartite lattice, namely $n = N_B - N_A > 0$, there are $n$ degenerate solutions with the eigenvalue $\epsilon_B$ (the on-site energy of the majority sublattice), with the wave functions residing entirely on this sublattice. This can be seen, from the following simple considerations, as an alternative to Pereira *et al's* proof that used the rank-nullity theorem in linear algebra [25].

We begin with the conjecture that there are some solutions where the wave functions live completely on the majority sublattice ($B$), and proceed to find them. Thus we have

$$\begin{pmatrix} \mathcal{H}_{BB} & \mathcal{H}_{BA} \\ \mathcal{H}_{BA}^{\dagger} & \mathcal{H}_{AA} \end{pmatrix} \begin{pmatrix} \Psi_B \\ 0 \end{pmatrix} = E \begin{pmatrix} \Psi_B \\ 0 \end{pmatrix}, \tag{3}$$

where $\Psi_B$ is a vector in the $B$ sublattice of dimension $N_B$ and there is null contribution from the $A$ sublattice to the wave function. It will be clear from the following discussion that for the theorem to hold, the $B$ sublattice $N_B \times N_B$ Hamiltonian is restricted to the diagonal form

$$\mathcal{H}_{BB} = \epsilon_B I, \tag{4}$$

and there are no restrictions on the remaining part of the Hamiltonian. The specific form of $\mathcal{H}_{BB}$ means that there is no site disorder, nor is there any interaction between the atoms on the $B$ sublattice (hence it will fail if interactions beyond the NN are present, which will produce a non-diagonal $\mathcal{H}_{BB}$). However, such restrictions need not apply to the $A$ sublattice, so that the $N_A \times N_A$ Hamiltonian $\mathcal{H}_{AA}$ for the minority sublattice can have diagonal disorder and also there is no restriction on the form of $\mathcal{H}_{BA}$ as well. This means that the $A$ sublattice atoms can interact between themselves and with the $B$ sublattice atoms as well without invalidating the theorem.

The wave function $\Psi_B$ thus satisfies

$$\mathcal{H}_{BB}\Psi_B = E\Psi_B, \tag{5}$$

$$\mathcal{H}^{\dagger}_{BA}\Psi_B = 0. \tag{6}$$

The first of these equations tells us that if conjectured solutions of the form $(\Psi_B, 0)$ exist, then they must have energy $E = \epsilon_B$ and there would be at most $N_B$ such degenerate solutions; the equation does not place any constraints on the individual components of $\Psi_B$.

Turning to equation (6), there are $N_B$ components of $\Psi_B$ to be determined but only $N_A < N_B$ equations to determine them. This means that the solutions cannot be fully determined. However, if we specify $N_B - N_A$ components of $\Psi_B$, then the remaining components are uniquely determined as linear functions of these components. These solutions are therefore of the form

$$\Psi_B = (\phi_1, \phi_2, \ldots, \phi_{N_B-N_A}; f_1, f_2, \ldots, f_{N_A}), \tag{7}$$

where we can choose the $\phi_i$'s arbitrarily and the $f_i$'s are then just linear combinations of $\phi_i$'s ($f_i = \sum_{j=1}^{N_B-N_A} c_{ij}\phi_j$, where the expansion coefficients are determined by $\mathcal{H}^{\dagger}_{BA}$ in equation (6)). Thus the number of linearly independent solutions is given by the number of ways in which we can choose linearly independent solutions in the subspace $(\phi_1, \phi_2, \ldots, \phi_{N_B-N_A})$, which is clearly $N_B - N_A$. This proves the conjecture and theorem.

It is easy to see why the theorem is not valid if there is on-site disorder on the majority sublattice or interactions beyond the NN, which introduces off-diagonal terms in $\mathcal{H}_{BB}$. So, equation (4) is no true longer. This means that equation (5) puts constraints on the components of $\Psi_B$ in order to satisfy the eigenvalue problem, and as a result equations (5) and (6) cannot both be satisfied simultaneously. For example, if we use the form equation (7) which satisfies equation (6), we are only left with the freedom to choose $\phi_1$, $\phi_2$, ..., $\phi_{N_B-N_A}$ and this is not enough to satisfy the eigenvalue problem of equation (5). There is no such problem if $\mathcal{H}_{BB} = \varepsilon_B I$, since any vector $(\phi_1, \phi_2, \ldots, \phi_{N_B-N_A}; f_1, f_2, \ldots, f_{N_A})$ is a solution with $E = \varepsilon_B$.

The theorem has an important bearing on the results of the supercell calculations, both tight-binding and density functional. In these calculations, the vacancies are repeated in each supercell, connected by the superlattice translational vectors, and hence are all located on the same sublattice, which forms the minority sublattice. If $n$ is the number of supercells in the crystal, then this is also the imbalance in the number of atoms in the two sublattices $n = N_B - N_A$. According to the theorem, there should be $n$ zero modes in the Brillouin zone, which is also precisely the number of Bloch momentum points in the Brillouin zone. These states thus show up in the form of a dispersionless band in the tight-binding supercell calculations at $E = 0$.

If hopping beyond the NN is present or if the on-site energies of the different atoms are different, then the theorem does not hold. However, the hopping beyond the NN in graphene is small [29] and the on-site energies are negligibly different on sites close to the vacancy as obtained from the DFT calculations. Because these effects are small, a clearly identifiable, nearly dispersionless zero-mode band is found in the DFT calculations as can be seen from figure 4, as well as in the higher-neighbor tight-binding results (figure 7), where the zero-mode band is marked by red dots.

### *4.2. Tight-binding results: direct diagonalization of the Hamiltonian*

In order to better understand the formation of zero-mode states, we have studied the vacancy $\pi$ bands with the standard tight-binding model of the $p_z$ orbitals containing both NN and 2NN

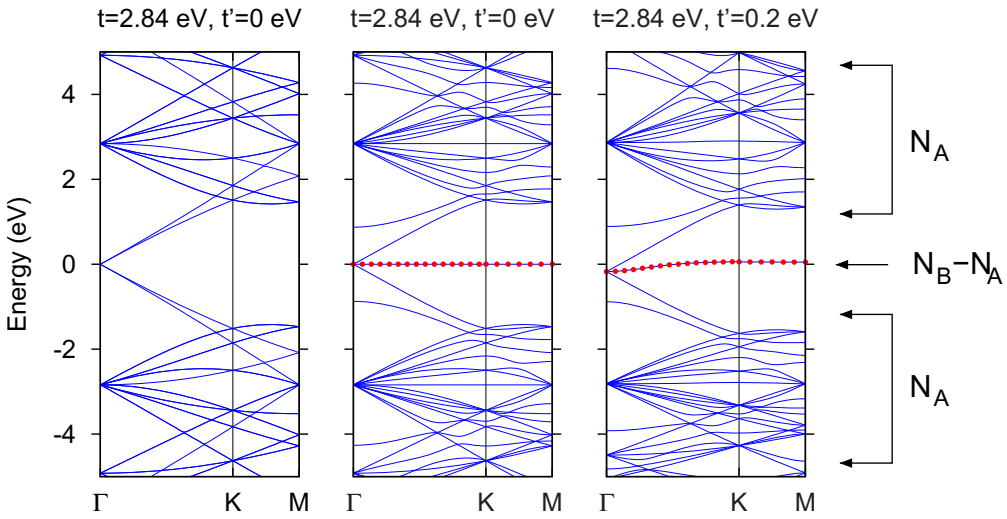


**Figure 7.** Tight-binding band structure obtained from the Hamiltonian equation (8) for the 72-atom $6 \times 6$ supercell both with and without a vacancy. The band structure without the vacancy is shown in the left panel. The Dirac points $K$ and $K'$ of the original graphene Brillouin zone get folded into the $\Gamma$ point of the supercell Brillouin zone and the two linear Dirac bands are clearly seen in the left panel. The middle and right panels show the zero-mode states (red dots) with and without the 2NN interaction $t'$. In the NN tight-binding approximation (middle panel), all zero modes have the same energy and live exclusively on the majority sublattice, whereas with the 2NN interaction, the zero-mode states have a band dispersion and leak into the minority sublattice as well. The sublattice with the vacancy atoms is labeled $A$ and the total number of states in different bands (not counting spin degeneracy) is shown on the right, with $N_A$ and $N_B$ denoting the total numbers of atoms in the two sublattices of the entire crystal.

interactions. In particular, we look for the vacancy-induced zero-mode states discussed in the previous subsection.

The tight-binding Hamiltonian is

$$\mathcal{H}_{\mathrm{TB}} = -t \sum_{\langle ij \rangle \sigma} c^{\dagger}_{i\sigma} c_{j\sigma} + t' \sum_{\langle\langle ij \rangle\rangle \sigma} c^{\dagger}_{i\sigma} c_{j\sigma} + \mathrm{h.c.}, \tag{8}$$

where $-t$ and $t'$ are the NN and 2NN interactions with the signs chosen such that $t, t' > 0$ ($t \approx 2.91\,\mathrm{eV}$ and $t' \approx 0.16\,\mathrm{eV}$ for graphene [29]).

The band structures and the DOSs are shown in figures 7 and 8. The electron counting in the band structure figure 7 is as follows. Both the lower and the upper bands contain in total (integrated over the Brillouin zone) $N_A$ states each, whereas the zero-mode band contains $N_B - N_A$ states, making a total of $N_A + N_B$ states, as must be the case. We have one $\pi$ electron per site present in the system, so that taking the spin into account, the entire lower subband is full, while the zero-mode states are half full. For the single vacancy ($N_B - N_A = 1$), this leads to a single occupied electron in the zero-mode states, resulting in $S = 1/2$ in agreement with Lieb's theorem [34].

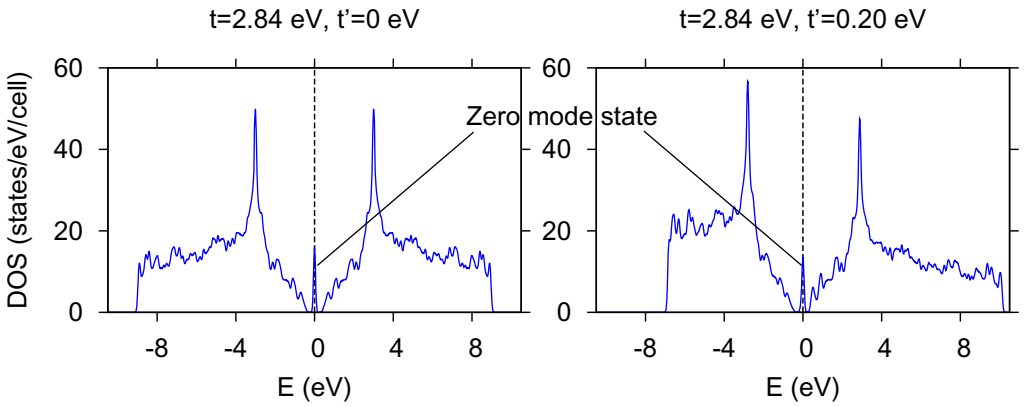


**Figure 8.** The tight-binding $\pi$ DOSs of graphene with a vacancy either with NN interactions alone (left) or with both NN and 2NN interactions present (right), as obtained from the tight-binding Hamiltonian equation (8).

As discussed in the previous section, if NN interactions alone are present, we should have $N_B - N_A$ zero-mode states at $E = 0$ exactly. That is why the zero-mode band in the middle panel of figure 7 is completely flat. However, if, in addition, 2NN interactions are also present, then the energies of the zero-mode states are not guaranteed to be the same and we see a spread in the energy of these states, which shows up as a dispersion in the zero-mode band, as seen from the right panel of figure 7.

Here, the vacancy site was modeled by simply removing a lattice site, corresponding to the vacancy potential $U_0 = \infty$. In a real material, however, $U_0$ is large but finite. The effect of a finite $U_0$ is that (i) it causes the zero-mode state to occur slightly below the mid-gap ($E = 0$) and (ii) the sharp zero-mode state turns into a resonance state due to interaction with the continuum $\pi$ bands. This can be best described with the GF approach discussed in the next subsection.

### *4.3. Impurity Green's function and the zero-mode state in the $\pi$ bands*

In this section, we investigate the effect of a single impurity on the $\pi$ electron states by studying Dyson's equation and show that the zero-mode state emerges as the strength of the impurity potential $U_0$ is gradually increased. For the vacancy, this potential is large but finite, so that the results obtained in this section are helpful in understanding the nature of the zero-mode state in the actual structure with a finite vacancy potential.

The wave function of the zero-mode state is obtained from the Lippmann–Schwinger equation. Consistent with previous results [25, 36], we find that (i) the zero-mode state consists of wave functions from the majority sublattice alone and (ii) it is quasi-localized decaying as $1/r$ as a function of distance from the vacancy in the limit of the linear-band approximation. In addition to these known results, our analysis allows us to (i) obtain the oscillatory phase factors in the zero-mode wave function due to the interference of the two Dirac points and (ii) compare the linear-dispersion results with the full tight-binding band result by computing the GFs for large distances in both cases.

The vacancy is modeled by adding an on-site perturbation $V$ to the unperturbed NN tight-binding Hamiltonian, so that

$$\mathcal{H} = \mathcal{H}_0 + V, \tag{9}$$

where $\mathcal{H}_0 = -t\sum c^{\dagger}_{i\alpha}c_{j\beta} + \text{h.c.}$, $i\alpha$ being the site-sublattice index, and

$$V = U_0 c^{\dagger}_{0A} c_{0A}, \tag{10}$$

where $U_0$ is the strength of the potential due to the impurity on the $A$-sublattice of the central cell. The vacancy corresponds to the value of $U_0 \to \infty$.

A key quantity of interest here is the unperturbed GF, $G^0(E) = (E + \mathrm{i}\eta - \mathcal{H}_0)^{-1}$, the calculation of which was discussed in our earlier paper that studied the Ruderman–Kittel–Kasuya–Yoshida (RKKY) interaction in graphene [37]. As usual, the imaginary part of the GF contains information about the DOS: $\rho^0(E) = -\pi^{-1}\mathrm{Im}\, G^0(E)$. The GF $G(E)$ in the presence of perturbation will be obtained from Dyson's equation.

Since we will be interested in the local density of states (LDOS) in the various carbon sites and how they are modified by the presence of an impurity, we need to calculate the real-space matrix elements $G^0_{i\alpha,j\beta}(E) \equiv \langle i\alpha|G^0(E)|j\beta\rangle$. This may be done by going to momentum space and defining the Bloch functions for the electrons $|\vec{k}\alpha\rangle = N^{-1/2}\sum_i \mathrm{e}^{\mathrm{i}\vec{k}\cdot\vec{r}_{i\alpha}}|i\alpha\rangle$, with $\vec{r}_{i\alpha} = \vec{R}_i + \vec{\tau}_\alpha$ being the position vector of the $\alpha$th atom in the $i$th unit cell. The unperturbed Hamiltonian $\mathcal{H}_0$ in this basis set becomes

$$\mathcal{H}_{\vec{k}} = \begin{pmatrix} 0 & f(\vec{k}) \\ f^*(\vec{k}) & 0 \end{pmatrix},$$

where $f(\vec{k}) = -t\ (\mathrm{e}^{\mathrm{i}\vec{k}\cdot\vec{d}_1} + \mathrm{e}^{\mathrm{i}\vec{k}\cdot\vec{d}_2} + \mathrm{e}^{\mathrm{i}\vec{k}\cdot\vec{d}_3})$ and $\vec{d}_1$, $\vec{d}_2$ and $\vec{d}_3$ are the positions of the three NNs. Diagonalization of the Hamiltonian yields the eigenenergies $E(\vec{k}) = \pm|f(\vec{k})|$, which when expanded around the Dirac points lead to the usual linear band structure $E(\vec{q}) = \pm v_{\mathrm{F}}|\vec{q}|$, where $\vec{q} = \vec{k} - \vec{K}_D$ is the deviation from the Dirac point in the Brillouin zone. Here the Fermi velocity $v_{\mathrm{F}} = 3ta/2$, where $a$ is the carbon–carbon bond length. Note that unlike in our previous work [37], $v_{\mathrm{F}}$ is defined here as a positive quantity, since $t$ is positive.

The real-space GFs are conveniently obtained by first calculating the momentum-space GF, which can be easily shown to be $G^0(\vec{k}E) \equiv \langle\vec{k}\alpha|G^0(E)|\vec{k}\beta\rangle = (E + \mathrm{i}\eta + \mathcal{H}_{\vec{k}})((E + \mathrm{i}\eta)^2 - |f(\vec{k})|^2)^{-1}$. A Fourier transform then yields the real-space unperturbed GF, namely

$$G^0_{i\alpha,j\beta}(E) = \frac{1}{N}\sum_{\vec{k}} \mathrm{e}^{\mathrm{i}\vec{k}\cdot(\vec{r}_{i\alpha} - \vec{r}_{j\beta})} G^0_{\alpha\beta}(\vec{k}E), \tag{11}$$

which can be calculated by a simple brute-force summation over the Brillouin zone. It can also be computed by a second method using the Horiguchi recursive technique [37, 38]. However, the latter, despite being computationally fast, has convergence problems [39] for distances $|\vec{R}_i - \vec{R}_j| \geqslant 7a$ so, in this case it is a better method to use only smaller distances.

The perturbed GF is related to the unperturbed GF through Dyson's equation: $G = G^0 + G^0\, VG$. Using the localized form of the impurity potential, equation (10), and taking the matrix elements, we immediately obtain, for the real-space GF, the result

$$G_{i\alpha,j\beta}(E) = G^0_{i\alpha,j\beta}(E) + U_0 \times G^0_{i\alpha,0A}(E) G_{0A,j\beta}(E). \tag{12}$$

We are specifically interested in the on-site GFs with $\alpha = \beta$ and $R_i = R_j$, which give the LDOS on the $A$ and $B$ sites at distance $r_{i\alpha} = R_i + \tau_\alpha$ from the impurity site. Equation (12) is easily inverted to yield the perturbed $G(E)$ in terms of the unperturbed $G^0(E)$, namely

$$G_{i\alpha,i\alpha}(E) = G^0_{i\alpha,i\alpha}(E) + \frac{U_0 G^0_{i\alpha,0A}(E) G^0_{0A,i\alpha}(E)}{1 - U_0 G^0_{0A,0A}(E)}. \tag{13}$$

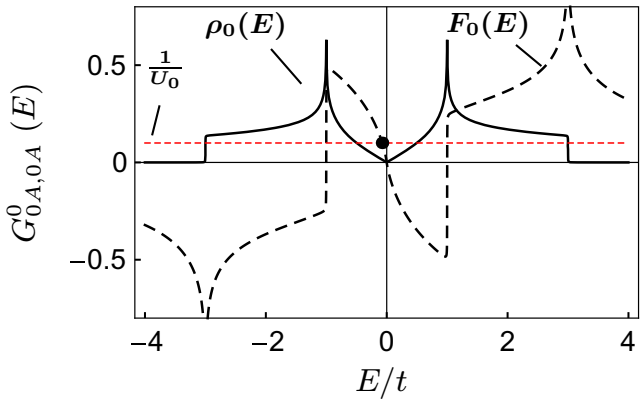


**Figure 9.** On-site GF $G^0_{0A,0A}(E)$ for the $\pi$ bands computed by the Horiguchi method and the energy of the resonance state, indicated by a black dot, obtained from Dyson's equation: $U_0F_0(E) = 1$. As $U_0 \to \infty$, the solution moves to $E \to 0$, leading to the sharply localized zero-mode state at the band center.

The LDOS at different sites may be obtained by taking the imaginary parts of the diagonal elements of the GF: $\rho_{i\alpha}(E) = -\pi^{-1}\mathrm{Im}\, G_{i\alpha,i\alpha}(E)$. It immediately follows from equation (13) that the LDOS at the impurity site has the much simpler form

$$\rho_{0A}(E) = \frac{\rho_0(E)}{(1 - U_0F_0(E))^2 + (\pi U_0\rho_0(E))^2}, \tag{14}$$

where $\rho_0(E) = -\pi^{-1}\,\mathrm{Im}\, G^0_{0A,0A}(E)$ is the unperturbed LDOS at the central site, which is of course the same for every site in unperturbed graphene, and $F_0(E) = \mathrm{Re}\, G^0_{0A,0A}(E)$. Note that we have defined here $\rho_0(E)$ to be the unperturbed DOS per sublattice per spin (which is independent of the sublattice or the cell index) and $\rho_{i\alpha}(E)$ is the corresponding perturbed quantity for the $i\alpha$ site.

The resonance condition follows from equation (14), namely

$$1 - U_0F_0(E_0) = 0, \tag{15}$$

where $E_0$ is the resonance energy. The graphical solution to this equation is shown in figure 9. There are four solutions for $E_0$: the two solutions at $E_0 = \pm t$ do not produce much change in the DOS, as may be inferred from equation (14), due to the diverging DOS $\rho_0(E)$ there, and the bound state with $E_0 \to U_0$ for large $U_0$ is inconsequential because it is removed to $\infty$, which then leaves the sole resonance state indicated by the black dot in figure 9. Its energy goes to 0 in the limit $U_0 \to \infty$ and the oscillator strength to 1, producing the zero-mode state for the vacancy.

The total DOS in the presence of the perturbation may be computed by taking the trace of equation (13) for the entire lattice. Using the identity $\sum_{i\alpha} G^0_{i\alpha,0A}(E)G^0_{0A,i\alpha}(E) = -\mathrm{d}G^0_{0A,0A}(E)/\mathrm{d}E$ and some tedious algebra, the result is

$$\rho_{\mathrm{tot}}(E) = 2\rho_0(E) + \frac{1}{N} \times \frac{-U_0[U_0\rho_0(E)F_0'(E) + \rho_0'(E)(1 - U_0F_0(E))]}{(1 - U_0F_0(E))^2 + (\pi U_0\rho_0(E))^2}. \tag{16}$$

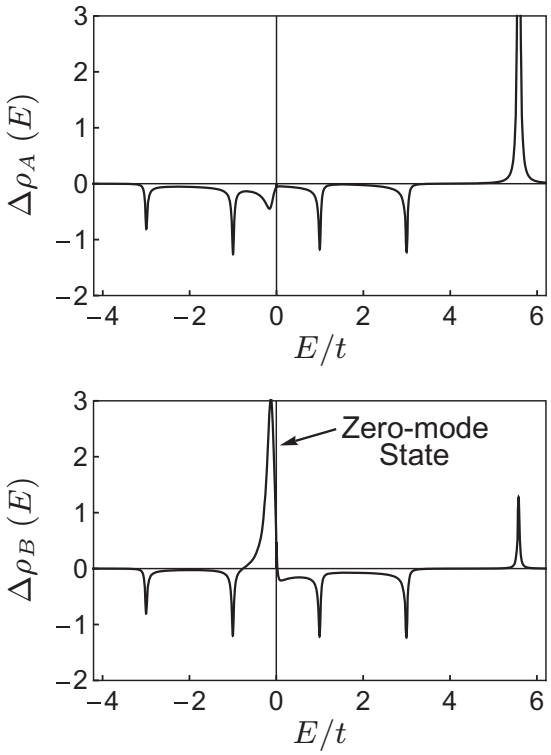


**Figure 10.** Changes in the total sublattice DOS due to the addition of the impurity with $U_0 = 5t$ as computed from the factors by multiplying the coefficient '$1/N$' in equations (17) and (18). The emergence of the zero-mode state on the $B$ sublattice at $E = 0$ is clearly seen, which grows into a $\delta$ function as $U_0 \to \infty$. The remaining changes in the DOS go to zero as $1/N$, except for the (unimportant) bound state on the $A$ sublattice (occurring at $E/t \sim 6$ in the top panel), which becomes a $\delta$-function bound state as $E \to \infty$ in the limit of $U_0 \to \infty$.

Similarly, by taking the trace of equation (13) over the cell index alone, the individual sublattice DOS may be found, which for the $A$ sublattice reads as

$$\rho_A(E) = \rho_0(E) + \frac{1}{N} \times \frac{-U_0[(1 - U_0 F^0(E))\mathrm{Im}\,\xi(E) - \pi U_0 \rho_0(E)\mathrm{Re}\xi(E)]}{\pi[(1 - U_0 F_0(E))^2 + (\pi U_0 \rho_0(E))^2]}, \tag{17}$$

where $\xi(E) = (1/N)\sum_k [G^0_{AA}(kE)]^2$ and the DOSs are, again, per sublattice and per spin. A similar expression for $\rho_B(E)$ reads

$$\rho_B(E) = \rho_0(E) + \frac{1}{N} \times \frac{-U_0[(1 - U_0 F^0(E))(\pi \rho_0'(E) - \mathrm{Im}\,\xi(E)) + \pi U_0 \rho_0(E)(F_0'(E) + \mathrm{Re}\,\xi(E))]}{\pi[(1 - U_0 F_0(E))^2 + (\pi U_0 \rho_0(E))^2]}. \tag{18}$$

It can be verified from equations (16)–(18) that $\rho_{\mathrm{tot}}(E) = \rho_A(E) + \rho_B(E)$, so that these equations are consistent.

The numerical results are summarized in figures 10–12. The factors multiplying the $1/N$ in equations (17) and (18) are the changes in the DOS $\Delta\rho_A(E)$ and $\Delta\rho_B(E)$ introduced by the

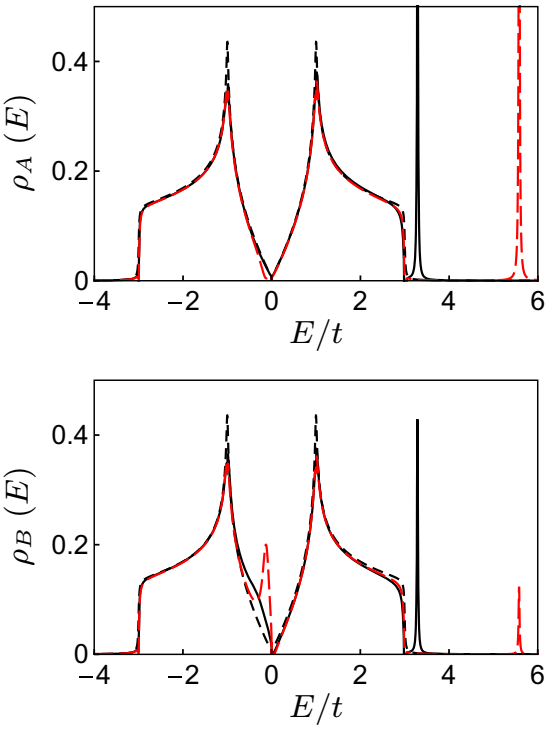


**Figure 11.** Total DOS for the $A$ sublattice $\rho_A(E)$ (top) and the $B$ sublattice $\rho_B(E)$ (bottom) for different values of the impurity potential $U_0/t = 0, 2$ and 5, denoted by black dashed, black solid and red dashed lines, respectively. These results are obtained from equations (17) and (18) by using $N = 20$ for the purpose of plotting. The figure shows the evolution of the zero-mode state at $E = 0$, which lives completely on the $B$ sublattice in the limit of $U_0 \to \infty$, i.e. opposite to the sublattice in which the vacancy is introduced.

impurity potential, which are shown in figure 10. Figure 11 shows the emergence of the zero mode in the DOS with $E = 0$ and that this state resides entirely on the $B$ sublattice in the limit $U_0 \to \infty$. Figure 12 shows the LDOS on the impurity site ($\rho_{0A}$) and on the nearest ($\rho_{0B}$) and the next-nearest sites ($\rho_{1A}$).

The width of the resonance peak increases with resonance energy $E_0$. Keeping the linear term in the expansion of $F_0(E)$, namely $F_0(E) \approx U_0^{-1} + F_0'(E_0)(E - E_0)$, equation (16) yields the Lorentzian lineshape

$$\rho_{\rm tot}(E) \approx 2\rho_0(E) + \frac{1}{\pi N}\frac{\Gamma}{(E - E_0)^2 + \Gamma^2}, \tag{19}$$

where the resonance width is given by

$$\Gamma = -\pi\rho_0(E_0)/F_0'(E_0). \tag{20}$$

The width is zero if $E_0 = 0$ and increases with energy as shown in figure 13.

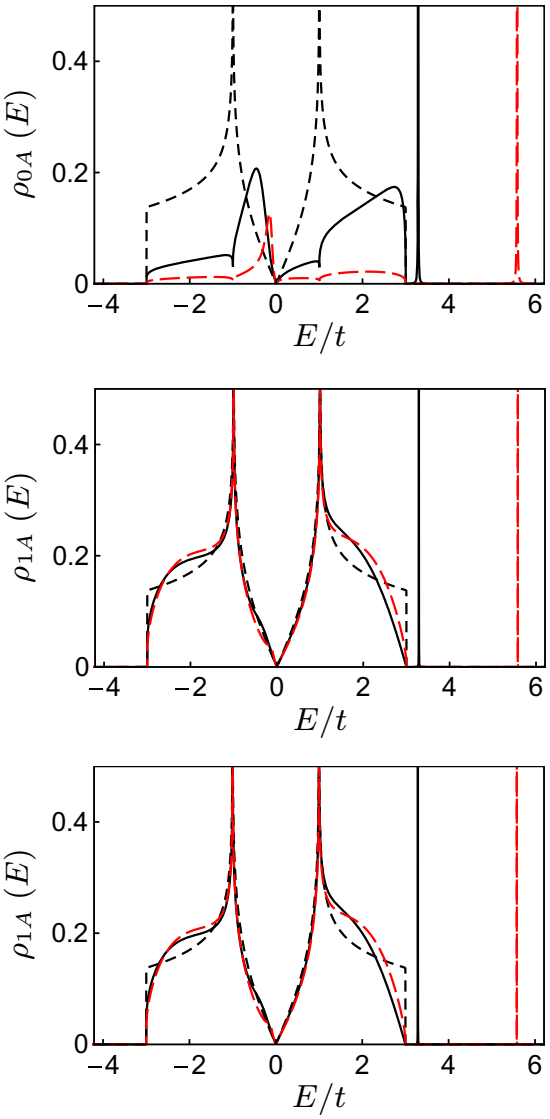


**Figure 12.** LDOS at the impurity site $\rho_{1A}$ (top), the NN site $\rho_{0B}$ (middle) and the next-NN site $\rho_{1A}$ (bottom) obtained from equations (13) and (14) for different strengths of the impurity potential $U_0/t = 0$, 2 and 5, denoted by black dashed, black solid and red dashed lines, respectively. As $U_0 \to \infty$, the top LDOS goes to zero (except for the bound state beyond the top of the band whose energy goes to $\infty$), and the zero-mode state lives only on the $B$ sublattice, as indicated by the middle and bottom panels. The prominent zero-mode peak in the middle panel for $U_0/t = 5$ will develop into a $\delta$-function peak at $E = 0$ as the impurity potential $U_0 \to \infty$.

### *4.4. Impurity state wave function*

In this section, we study the impurity state $V\pi$ wave function from the Lippmann–Schwinger equation. The analysis allows us to obtain the well-known $1/r$ decay of the vacancy state;

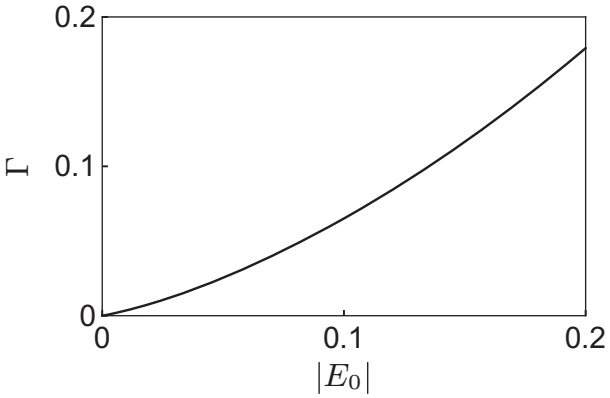


**Figure 13.** Resonance width of the zero-mode state ($V\pi$) as a function of the resonance energy $E_0$. Both $E_0$ and $\Gamma$ are in units of the NN hopping, with the value $t \approx 2.56\,\mathrm{eV}$ [29] if the NN hopping alone is kept.

however, in addition we also obtain the oscillatory behavior of the wave function due to the interference between the two Dirac cones.

Our starting point is the Lippmann–Schwinger equation $|\Psi\rangle = |\Psi^0\rangle + G^0\, V|\Psi\rangle$, where $|\Psi^0\rangle$ is the unperturbed state. For the localized impurity potential on the central $A$ site, $V = U_0|0A\rangle\langle 0A|$, the Lippmann–Schwinger equation leads to the wave function

$$\Psi_{i\alpha} \equiv \langle i\alpha|\Psi\rangle = \Psi^0_{i\alpha} + \frac{U_0 G^0_{i\alpha,0A}(E)\Psi^0_{0A}}{1 - U_0 G^0_{0A,0A}(E)}. \tag{21}$$

We are interested in the low-energy behavior, since that is the region where the resonance state gets introduced by the impurity as seen from figure 9. The GFs for the full tight-binding band structure as well as for the linear bands were computed in our previous work [37]. For the linear bands and in the low-energy limit, the results are

$$\begin{aligned} G^0_{iA,0A}(E) &= -\beta \frac{A_c E}{2\pi v_F^2} K_0\left(\frac{-\mathrm{i}Er}{v_F}\right), \\ G^0_{iB,0A}(E) &= \alpha \frac{A_c E}{2\pi v_F^2} K_1\left(\frac{-\mathrm{i}Er}{v_F}\right), \end{aligned} \tag{22}$$

where $A_c$ is the unit cell area in graphene, $K_0$ and $K_1$ are the modified Bessel functions of the second kind and $\vec{r}$ is the distance vector between the two atoms: $\vec{r} = \vec{r}_{iA} - \vec{r}_{0A}$ for the first GF and $\vec{r} = \vec{r}_{iB} - \vec{r}_{0A}$ for the second. The multiplicative factors are $\beta = \mathrm{e}^{\mathrm{i}\vec{K}\cdot\vec{r}} + \mathrm{e}^{\mathrm{i}\vec{K}'\cdot\vec{r}}$, which is a real number for the graphene lattice, and

$$\alpha = \mathrm{e}^{-\mathrm{i}\pi/3}(\mathrm{e}^{\mathrm{i}(\vec{K}\cdot\vec{r}-\theta_r)} - \mathrm{e}^{\mathrm{i}(\vec{K}'\cdot\vec{r}+\theta_r)}), \tag{23}$$

which is purely imaginary, and the polar angle $\theta_r = \tan^{-1}(y/x)$ is defined with the $x$-direction taken to be along the vector $\vec{K}' - \vec{K}$, which are two adjacent Dirac points in the Brillouin zone.

Using the small $z$ expansion for the Bessel functions [40]: $K_0(z) = -\ln(z/2) - \gamma$ and $K_1(z) = z^{-1} + 2^{-1} z \ln(z/2) + (\gamma - 1/2)z/2$, where $\gamma \approx 0.577$ is the Euler–Mascheroni constant,

we find that the Bessel functions entering the expressions for the GFs (equation (22)) become, in the low-energy limit,

$$K_0\left(-\frac{\mathrm{i}Er}{v_\mathrm{F}}\right) = \frac{\mathrm{i}\pi}{2}\mathrm{sign}(E) + \ln\frac{2v_\mathrm{F}}{|E|r} - \gamma,$$
$$K_1\left(-\frac{\mathrm{i}Er}{v_\mathrm{F}}\right) = -\frac{v_\mathrm{F}}{\mathrm{i}Er} - \frac{\mathrm{i}Er}{2v_\mathrm{F}}\ln\left(-\frac{\mathrm{i}Er}{2v_\mathrm{F}}\right) - \left(\gamma - \frac{1}{2}\right)\frac{\mathrm{i}Er}{2v_\mathrm{F}}. \tag{24}$$

Plugging these into equation (22), taking the $E \to 0$ limit and retaining the lowest-order terms in energy, we find the following results:

$$G^0_{iA,0A}(E) = \frac{A_\mathrm{c}\beta}{2\pi v_\mathrm{F}^2} \times \left(E\ln\frac{|E|r}{2v_\mathrm{F}} + \gamma E - \frac{\mathrm{i}\pi}{2}|E|\right),$$
$$G^0_{iB,0A}(E) = \frac{A_\mathrm{c}\,\mathrm{Im}\,\alpha}{2\pi v_\mathrm{F}^2}\left[-\frac{v_\mathrm{F}}{r} + \frac{E^2 r}{2v_\mathrm{F}}\left(\gamma - 2^{-1} + \ln\frac{|E|r}{2v_\mathrm{F}}\right) - \frac{\mathrm{i}r\pi}{4v_\mathrm{F}}E^2\,\mathrm{sign}\,E\right]. \tag{25}$$

There is no guarantee that these results, calculated for the linear bands extending to infinite energy, should agree even for low energies with the GFs for the actual bands, e.g. as obtained with the tight-binding band structure. Certain elements must exactly agree at low energies, for example, the imaginary part of $G^0_{0A,0A}$, which yields the DOS, since at low energies, it is controlled by the Fermi velocity $v_\mathrm{F}$ alone. We, nevertheless, find that expressions (25) agree quite well with the tight-binding GFs, the agreement becoming better with increasing distance. A comparison between the low-energy GFs, equations (25), and the full GFs for a typical case is shown in figure 14, which illustrates the symmetry of the GFs. A notable exception is the real part of the on-site GF $G^0_{0A,0A}(E)$, where the substitution of $r = 0$ into equation (25) yields a divergent result. However, we find that the tight-binding GF in this case can be fitted to expression (25) for $G^0_{0A,0A}(E)$, provided that we use the value $r \approx 0.6a$ instead of $r = 0$.

We note that the symmetry properties of the above GF equations (25) are consistent with the results [38] that follow from the particle–hole symmetry and are valid for all energies, namely $\mathrm{Re}\,G^0_{i\alpha,j\beta}(E) = \pm\mathrm{Re}\,G^0_{j\beta,i\alpha}(E)$, $\mathrm{Im}\;G^0_{i\alpha,j\beta}(E) = \pm\mathrm{Im}\,G^0_{j\beta,i\alpha}(E)$ and $G^0_{i\alpha,j\beta}(E) = G^0_{j\beta,i\alpha}(E)$, where the upper (lower) sign is for $\alpha = (\neq)\beta$. The symmetry properties for specific cases are illustrated in figure 14.

The nature of the impurity state immediately follows from the Lippmann–Schwinger expression (21). First of all, note an important point from the expression for the GF equations (25), namely that all GFs vanish at $E = 0$ except for the real part of $G^0_{iB,0A}$, which is finite and decays as $1/r$. This is precisely the reason for the property that the zero-mode state resides on the majority sublattice $B$ alone and its wave function decays inversely with distance. These features hold true if NN interactions alone are present on the graphene lattice. If 2NN interactions are present, then there is no electron–hole symmetry and the behavior of the GFs near the resonance energy differs from equation (25). The form of the GFs for the latter case is such that *both* sublattices contribute to the resonance state near $E = 0$, an issue that is discussed in detail elsewhere [41].

Returning to the Lippmann–Schwinger equation (21) and inserting into it the low-energy expansion for the GFs (equation (25)) and then taking the limit of the resonance energy $E_0 = 0$, it can be easily seen that as $E_0 \to 0$ in the limit $U_0 \to \infty$, the impurity wave function follows the behavior

$$\Psi = \begin{pmatrix}\Psi_{iA}\\ \Psi_{iB}\end{pmatrix} = \begin{pmatrix}1/\ln|E_0|\\ c_i|E_0|^{-1}\end{pmatrix} \to \begin{pmatrix}0\\ c_i\end{pmatrix}. \tag{26}$$

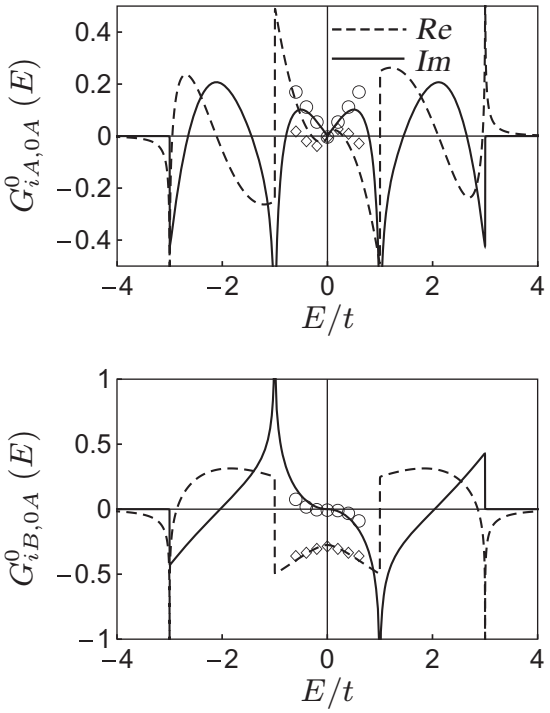


**Figure 14.** Illustration of the symmetry of the GF and its low-energy behavior, calculated using the Horiguchi method and the tight-binding band structure. Dashed and full lines denote the real and imaginary parts, respectively. For the upper panel, the distance vector of the atom with respect to the impurity is given by $\vec{r} = \vec{r}_{iA} - \vec{r}_{0A} = 2\sqrt{3}a(1, 0)$, whereas for the lower panel, it is $\vec{r} = \vec{r}_{iB} - \vec{r}_{0A} = 2a(0, 1)$, where the coordinates are indicated in figure 6. The points near $E = 0$ are the low-energy results for the linear bands as given by equation (25).

This is an important result, which states that in the NN approximation, only the $B$ sublattice component survives for the zero-mode state, it being the stronger infinity. The surviving component is found to be simply proportional to the real part of the inter-sublattice GF,

$$\Psi_{iB} \propto \mathrm{Re}\, G^0_{iB,0A}(E_0 \to 0), \tag{27}$$

since its imaginary part vanishes. Using equation (25) and evaluating $\mathrm{Im}\,\alpha$ from equation (23), we finally obtained the desired result

$$\Psi_B(r) = \frac{N}{r} \sin[(\vec{K} - \vec{K}') \cdot \vec{r}/2 - \theta_r] \cos[(\vec{K} + \vec{K}') \cdot \vec{r}/2 - \pi/3], \tag{28}$$

where we have suppressed the cell index $i$, $N$ is a constant, $r$ is again the actual distance vector of the $B$ site with respect to the impurity position and the two Dirac points in the Brillouin zone may be taken as $K = 2\pi a^{-1}3^{-3/2}(-1, \sqrt{3})$ and $K' = 2\pi a^{-1}3^{-3/2}(1, \sqrt{3})$.

Equation (28) is the central result of this subsection that describes the $1/r$ decay of the vacancy-induced $V\pi$ state along with the phase factors. The long-range nature $1/r$ of the wave function (28) is well known [36], but the oscillatory factor due to the interference effect of the two Dirac points is new. The same kind of interference is also present in the oscillations of the RKKY interactions [37, 42]. The wave function is not square integrable because we used the

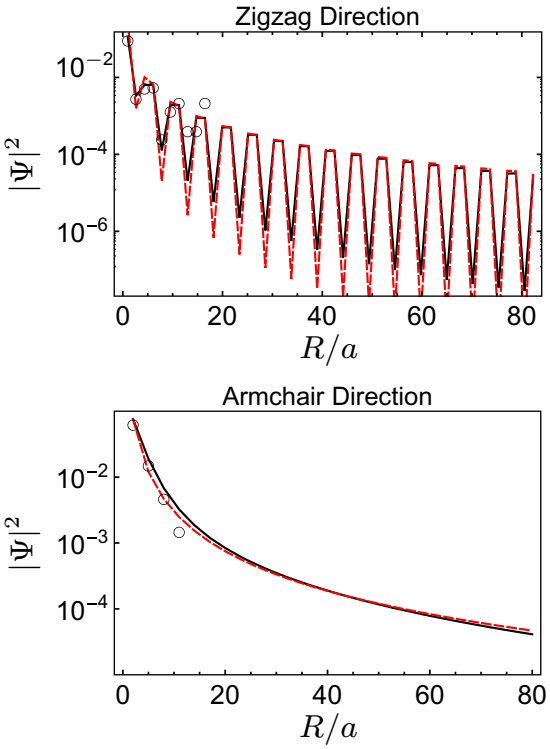


**Figure 15.** Square amplitude $|\Psi|^2$ of the zero-mode state on the $B$ sublattice along the zigzag and armchair directions computed from the Lippmann–Schwinger result equation (27) using GFs obtained for (a) the full tight-binding bands (black solid lines) and (b) linear bands (analytical expression, equation (28)) (red dashed lines). Circles indicate the same quantity computed from direct diagonalization of the tight-binding Hamiltonian on a finite lattice consisting of a single vacancy in a 512-atom supercell.

linear band structure, but it will be if we take into account the full band structure. Equation (28), nevertheless, describes the gross features of the zero-mode state. The wave function changes sign along different directions, e.g. it changes sign along the zigzag direction but not along the armchair direction. The kinetic energy gained by the delocalization of the wave function is exactly canceled by anti-bonding components present in the wave function, so that its energy is still equal to the on-site energy in spite of the delocalization. The calculated wave function for the zero-mode state is shown in figure 15. We note that a recent study has shown that the $1/r$ decay of the vacancy state remains unchanged even when a repulsive Coulomb interaction is included in the tight-binding Hamiltonian [43].

## 5. Summary

In summary, we have studied the electronic structure of graphene with a single substitutional vacancy from density-functional calculations using the all-electron LAPW method and interpreted the results with the help of the tight-binding model and the impurity GF approach. We find that the vacancy induces four localized states, namely three $V\sigma$ dangling bond states on

the carbon triangle and one $V\pi$ resonance state. The dangling bond states cause a Jahn–Teller distortion, which we found to be a planar distortion of the carbon triangle. Hund's coupling between these electrons would then produce the $S = 1$ state at the vacancy center as indicated in the summary figure (figure 1). The magnetic moment has two components: (i) the component $2\mu_B$ coming from the localized vacancy states $V\sigma$ and $V\pi$; and (ii) an opposite component of several tenths of $\mu_B$ coming from the spin polarization of the continuum $\pi$ band states in the vicinity of the vacancy. The second part is not well described in the supercell band calculations due to the slow $1/r$ decay of the 'quasi-localized' $V\pi$ wave function. This long-range decay also means that in an experimental sample it is only for extremely low vacancy concentration that the truly isolated vacancy limit is reached and as a result the magnetic moment is expected to be dependent on the vacancy concentration.

In addition to density-functional calculations, we also studied the formation of the $V\pi$ state in detail using the impurity GF approach for the isolated vacancy, which provided significant insight into the interpretation of the results of band calculations and the formation of zero-mode states in the $\pi$ bands. This zero-mode state is a slowly decaying localized state that lives mostly in the majority sublattice. It spreads into the minority sublattice (the one containing the vacancy) and becomes a resonance state due to the second and higher-neighbor interactions as well as the finite strength of the vacancy potential. The GF approach provided a sinusoidal phase factor associated with the $V\pi$ wave function described by equation (28). In addition to an understanding of the vacancy electronic structure, our work provides important insight necessary for the understanding of impurities in general, such as iron and cobalt dopants and other complex defects.

## Acknowledgment

This work was supported by the US Department of Energy through grant no. DOE-FG02-00ER45818.

## References

[1] Castro Neto A H, Guinea F, Peres N M R, Novoselov K S and Geim A K 2009 *Rev. Mod. Phys.* **81** 109
[2] Abergel D S L, Apalkov V, Berashevich J, Ziegler K and Chakraborty T 2010 *Adv. Phys.* **59** 261
[3] Bhattacharya A, Bhattacharya S, Majumder C and Das G P 2010 *J. Phys. Chem.* C **114** 10297
[4] Hashimoto A, Suenaga K, Gloter A, Urita K and Iijima S 2004 *Nature* **430** 870
[5] Ewels C P, Telling R H, El-barbary A A, Heggie M I and Briddon P R 2003 *Phys. Rev. Lett.* **91** 25505
[6] Nortlund K, Keinonen J and Matilla T 1996 *Phys. Rev. Lett.* **77** 699
[7] Esquinazi P, Spemann D, Höhne R, Setzer A, Han K-H and Butz T 2003 *Phys. Rev. Lett.* **91** 227201
[8] Kushmeric J G, Kelly K F, Rust H-P, Halas N J and Weiss P S 1999 *J. Phys. Chem.* B **103** 1619
[9] Barzola-Quiquia J, Esquinazi P, Rothermel M, Spemann D, Butz T and Garcia N 2007 *Phys. Rev.* B **76** 161403
[10] Ugeda M M, Brihuega I, Guinea F and Gómez-Rodríguez J M 2010 *Phys. Rev. Lett.* **104** 096804
[11] Červenka J, Katsnelson M I and Flipse J C F 2009 *Nature Phys.* **5** 840
[12] El-Barbary A A, Telling R H, Ewels C P, Heggie M I and Briddon P R 2003 *Phys. Rev.* B **68** 144107
[13] Yazyev O V and Helm L 2007 *Phys. Rev.* B **75** 125408
[14] Choi S, Jeong B W, Kim S and Kim G 2008 *J. Phys.: Condens. Matter* **20** 235220
[15] Singh R and Kroll P 2009 *J. Phys.: Condens. Matter* **21** 196002
[16] Yang X, Xia H, Qin X, Li W, Dai Y, Liu X, Zhao M, Xia Y, Yan S and Wang B 2009 *Carbon* **47** 1399

[17] Faccio R, Fernández-Werner L, Pardo H, Goyenola C, Ventura O N and Mombrú A W 2010 *J. Phys. Chem.* C **114** 18961
[18] Telling R H, Ewels C P, El-Barbary A A and Heggie M I 2003 *Nature Mater.* **2** 333
[19] Lehtinen P O, Foster A S, Ma Y, Krasheninnikov A V and Nieminen R M 2004 *Phys. Rev. Lett.* **93** 187202
[20] Ma Y, Lehtinen P O, Foster A S and Nieminen R M 2004 *New J. Phys.* **6** 68
[21] Lim D-H, Negreira A S and Wilcox J 2011 *J. Phys. Chem.* C **115** 8961
[22] Dai X Q, Zhao J H, Xie M H, Tang Y N, Li Y H and Zhao B 2011 *Eur. Phys. J.* B **80** 343
[23] Forte G, Grassi A, Lombardo G M, La Magna A, Angilella G G N, Pucci R and Vilardi R 2008 *Phys. Lett.* A **372** 6168
[24] Palacios J J and Ynduráin F 2012 arXiv:1203.6485v1
[25] Pereira V M, Lopes dos Santos J M B and Castro Neto A H 2008 *Phys. Rev.* B **77** 115109
[26] Hjort M and Stafström S 2000 *Phys. Rev.* B **61** 14089
[27] Palacios J J, Fernández-Rossier J and Brey L 2008 *Phys. Rev.* B **77** 195428
[28] Wu M, Cao C and Jiang J Z 2010 *New J. Phys.* **12** 063020
[29] Nanda B R K and Satpathy S 2009 *Phys. Rev.* B **80** 164530
[30] Blaha P *et al* 2001 *WIEN2k: An Augmented Plane Wave + Local Orbitals Program for Calculating Crystal Properties* (Austria: Karlheinz Schwarz, Techn. Universitat Wien)
[31] Perdew J P, Burke S and Ernzerhof M 1996 *Phys. Rev. Lett.* **77** 3865
[32] Grosso G and Parravicini P 2000 *Solid State Physics* (London: Academic)
[33] Thrower P A and Mayer R M 1978 *Phys. Status Solidi* a **47** 11
[34] Lieb E H 1989 *Phys. Rev. Lett.* **62** 1201
[35] Popovic Z S, Nanda B R K and Satpathy S 2012 (in preparation)
[36] Pereira V M, Guinea F, Lopes dos Santos J M B, Peres N M R and Castro Neto A H 2006 *Phys. Rev. Lett.* **96** 036801
[37] Sherafati M and Satpathy S 2011 *Phys. Rev.* B **83** 165425
Sherafati M and Satpathy S 2011 *Phys. Rev.* B **84** 125416
[38] Horiguchi T 1972 *J. Math. Phys.* **13** 1411
[39] Berciu M 2009 *J. Phys. A: Math. Theor.* **42** 395207
[40] Gradshteyn I S and Ryzhik I M 1980 *Tables of Integrals, Series, and Products* (New York: Academic) section 8.446
[41] Sherafati M and Satpathy S 2011 *Phys. Status Solidi* b **248** 2056
[42] Saremi S 2007 *Phys. Rev.* B **76** 184430
[43] Chang Y C and Haas S 2011 *Phys. Rev.* B **83** 085406